NANO · MICRO small
www.small-journal.com

Influence of Pore Architecture and Chemical Structure on the Sodium Storage in Nitrogen-Doped Hard Carbons

*Konstantin Schutjajew, Jonas Pampel, Wuyong Zhang, Markus Antonietti, and Martin Oschatz**

Hard carbon is the material of choice for sodium ion battery anodes. Capacities comparable to those of lithium/graphite can be reached, but the understanding of the underlying sodium storage mechanisms remains fragmentary. A two-step process is commonly observed, where sodium first adsorbs to polar sites of the carbon ("sloping region") and subsequently fills small voids in the material ("plateau region"). To study the impact of nitrogen functionalities and pore geometry on sodium storage, a systematic series of nitrogen-doped hard carbons is synthesized. The nitrogen content is found to contribute to sloping capacity by binding sodium ions at edges and defects, whereas higher plateau capacities are found for materials with less nitrogen content and more extensive graphene layers, suggesting the formation of 2D sodium structures stabilized by graphene-like pore walls. In fact, up to 84% of the plateau capacity is measured at potentials less than 0 V versus metallic Na, that is, quasimetallic sodium can be stabilized in such structure motifs. Finally, gas physisorption measurements are related to charge–discharge data to identify the energy storage relevant pore architectures. Interestingly, these are pores inaccessible to probe gases and electrolytes, suggesting a new view on such "closed pores" required for efficient sodium storage.

1. Introduction

The current energy change toward renewable electricity requires novel energy storage on a new scale. The discovery of graphite as an excellent and abundant lithium storage medium brought the lithium ion battery (LIB) to commercialization in the 1990s.[1] As a consequence of extensive research activities and size-scaling effects, LIBs became safer, smaller, cheaper, and found their way into almost every portable device of our daily life. Unfortunately, this trend is unlikely to continue in the future, because of limited lithium resources, as well as severe environmental and geopolitical issues arising from the mining of minerals required for LIB production. Hence, an alternative to LIBs is needed, which meets the high standards set by the LIB technology, particularly the high energy and power density as well as operational safety. One of the most promising strategies to achieve this goal is the use of the next heavier alkaline metal, sodium. The obvious advantages of sodium ion batteries (SIBs) over other alternative battery systems are their comparable operational voltage and largely similar chemical characteristics. More importantly, not only sodium itself is much more abundant than lithium but also cathode materials for SIBs are available which are safer and more abundant than their lithium counterparts.[2–8]

However, lithium and sodium do not behave identically when it comes to intercalation, for example, into graphite. In short terms, lithium can form the chemical compound LiC_6 with graphite due to high covalent contributions to the Li—C bond. Sodium is more ionic in bonding and lacks the ability to form covalent bonds with carbon. This takes the possibility to form stable binary intercalation compounds with non-expanded and heteroatom-free graphite.[9–12] More recently, hard carbon materials already known from LIB research were transferred to sodium ion anodes. Hard carbons are much more heterogeneous than graphite anodes, full of porosity and edge terminations, and consequently also their sodium storage mechanism is more complex and less well understood.

Sodiation of such materials is usually observed to proceed via several steps. First, defects and edge sites with high sodium adsorption enthalpy effectively stabilize and bind sodium ions at more positive potentials than bulk Na reduction. Due to Coulomb repulsion between the sodium ions and the corresponding mirror electrons located in the carbon, this occurs with a sloping potential, and in the corresponding sodiation curves, this process becomes apparent in form of a "sloping" region, that is, a steady decrease of the potential with increasing

K. Schutjajew,[+] Dr. J. Pampel,[++] W. Zhang, Prof. M. Antonietti, Prof. M. Oschatz[+]
Department of Colloid Chemistry
Max Planck Institute of Colloids and Interfaces
Am Mühlenberg 1, 14476 Potsdam, Germany
E-mail: martin.oschatz@uni-jena.de

The ORCID identification number(s) for the author(s) of this article can be found under https://doi.org/10.1002/smll.202006767.

[+]Present address: Friedrich-Schiller-University Jena, Institute for Technical Chemistry and Environmental Chemistry, Center for Energy and Environmental Chemistry Jena (CEEC Jena), Philosophenweg 7a, 07743 Jena, Germany

[++]Present address: Bundesanstalt für Materialforschung und –prüfung (BAM), Unter den Eichen 44-46, 12203 Berlin, Germany

DOI: 10.1002/smll.202006767

sodiation degree, similar to the storage mechanism in a capacitor or the formation of a solid solution.[13–15] When this effect exceeds the voltage for sodium reduction, the occupation of micropores occurs at potentials slightly more positive than 0 V versus Na/Na^+ where metallic sodium atoms and clusters are included. This process yields a sodiation capacity at rather constant potential close to that of metallic sodium. In the transition range between sloping and plateau, some authors report that intercalation between graphite-like domains of the hard carbon contributes to the capacity as well.[10–12] Finally, under overpotential conditions, sodium starts to deposit in a metallic state after a crystallization overpotential peak is overcome .[16] The process of bulk metal plating (i.e., the formation of large crystalline metal domains) is sometimes irreversible, considered unsafe, and is usually not operated.

The contribution of each process to sodium storage is governed by the textural and chemical properties such as the pore architecture and the bonding schemes of the electrode materials. A high amount of edges and defects will favor Na^+ adsorption and extend the sloping region, while in order to deposit sodium in an elemental state as atoms and sodium clusters at potentials less negative than the bulk, the presence of suitable nucleation sites and cavities is required. Formation of small sodium clusters is desirable for high-energy battery anodes because it enables safe operation at highly negative potentials. To our understanding, this storage mechanism might occur within small micropores, which usually either have very narrow apertures or are completely closed. Such pores could remain barely accessible to gas physisorption methods such as nitrogen or argon sorption at cryogenic temperatures, which are commonly applied for the characterization of pore networks.[17]

In order to link carbon structural properties to sodium storage mechanisms and to investigate the individual contributions independently of each other, the use of model compounds with adjustable and defined properties is desirable. Hydrocarbon-derived carbons or activated carbons often have ill-defined pore structure and atomic construction and are thus not applicable for that purpose. Hydrothermal synthesis[18–20] and templating approaches[21,22] or the fabrication of composite materials[23,24] can overcome at least part of the textural limitations but the resulting chemical structures after heating to high temperature remains confined within a narrow range. Therefore, specially selected carbon precursors, which follow a different but defined reaction pathway during pyrolysis and finally result in alternative materials, can serve as ideal model compounds.

Hexaazatriphenylene hexacarbonitrile (HAT-CN) is such a compound. It is only sp and sp^2 conjugated (thereby lacks sp^3-carbons), does not contain any hydrogen from the beginning, and polycondenses via a nitrile elimination/cyclization reaction.[25–27] For instance, Yan et al. already applied all-carbon composites containing condensed HAT-CN to investigate the fundamental mechanisms of charge storage in sodium-ion capacitor anodes. Conclusions on the influence of heteroatom-sites, pore structures, and composite structures on sodium have been drawn under operating conditions as typically applied in supercapacitors.[28,29]

To shift the focus from capacitive sodium ion storage under high power conditions to those more relevant for SIBs, the present work emphasizes the investigation of the processes at potentials close to metallic sodium under typical battery operating conditions. HAT-CN has been pyrolyzed in the temperature range between 550 and 1600 °C yielding carbons with comparable particle size and shape but with different pore structures, heteroatom content, and degree of carbon stacking. The presence of very small pores is investigated with physisorption using different probe gasses, showing that Ar physisorption most likely underestimates the total pore volume possibly accessible to the electrolyte as evaluated by capacity originating from irreversible formation of the solid–electrolyte-interface (SEI). The results further suggest the necessity to move away from the idea that results of physisorption methods allow deductions on the sodium storage properties. Full sodium uptake of the electrode materials was determined by lifting the often chosen but arbitrary potential limit of 0 V versus Na/Na^+ and sodiating the anode until bulk plating occurred. Thus, capacity at potentials slightly more negative than bulk sodium is considered as well, and sodium storage capacity is by that determined under all possible conditions. Sodium storage mechanisms under these conditions can be related to the model carbons' structural properties, and the relation between gas physisorption and electrochemical behavior reveals finer details of the loci and modes of charge storage.

2. Results and Discussion

2.1. Structural Characterization

The microporous carbonaceous materials studied in the present work are obtained by thermally induced condensation of HAT-CN.[25] The pore structure and heteroatom content, arguably the most crucial characteristics determining sodium storage properties of the resulting materials, are strongly dependent on the applied condensation temperature.

In order to assess the pore structure of the synthesized materials Ar sorption isotherms were measured at 87 K. It is widely accepted that Ar is the adsorptive of choice when dealing with heteroatom-rich adsorbents like those encountered in this work, because contrary to, for example, N_2, Ar lacks a quadrupole moment and therefore does not exhibit specific interactions with heteroatoms and other energetically heterogeneous areas on the material's surface.[30] The higher boiling point further gives rise to better resolved isotherms and increases diffusion rates.[31] As presented in **Figure 1**a, a IUPAC type I(a) isotherm with a steep uptake in the low relative pressure range is observed for both, C-HAT-550 and C-HAT-1000. C-HAT-550 additionally shows a type H4 hysteresis loop, which in combination with the type I(a) isotherm indicates a considerable amount of "inkbottle" pores (i.e., pores that are only accessible via small necks), inhibiting the equilibrium desorption of Ar. This "cavitation effect" is less pronounced in the isotherms of materials obtained at higher temperatures. C-HAT-1000 has a higher total Ar uptake with broader distribution over the low relative pressure range compared to C-HAT-550, revealing a higher volume of slightly larger micropores in C-HAT-1000. This is confirmed by the DFT-pore size distributions of the materials in Figure 1b,c, which show that the pore volumes of C-HAT-550 and C-HAT-1000 are dominated by small micropores with narrow size distribution centered around 1.0

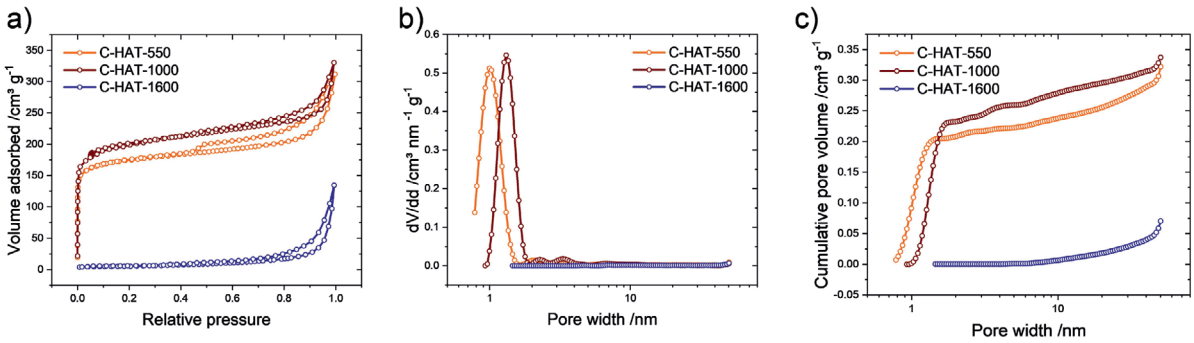

Figure 1. a) Ar-physisorption isotherms at 87 K. b) Differential pore size distribution and c) cumulative pore volume as calculated from QSDFT.

and 1.3 nm, respectively. The specific surface areas (SSAs) of C-HAT-550 and C-HAT-1000 as determined by the BET as well as the DFT model are summarized in **Table 1** and have similar values around 700 $m^2\ g^{-1}$ for both materials. C-HAT-1600 exhibits a type III isotherm, as it is typical for materials with low nanoporosity and prevalent external surface area. Consequently, the detected SSA is as low as 20 $m^2\ g^{-1}$ and arises mainly from adsorption on the external particle surface at high relative pressure. It is worth noting, that even though the area accessible to Ar dropped significantly, the pore volume available for the adsorption of CO_2 at 273 K reduced by only ≈25% after heating to 1600 °C, which means that during the second heat treatment the porosity did not collapse completely. As the heteroatom content is negligible in C-HAT-1600, the size of the remaining pores can be estimated from CO_2 physisorption by an NLDFT fit, yielding an average pore size of 0.6 nm (see Table 1 and Figure S1, Supporting Information). The presence of such pores after thermal treatment is in stark contrast to the behavior of carbohydrate derived hard carbons, where at a carbonization temperature of 1600 °C no CO_2 porosity is left.[32] From the present physisorption data C-HAT-1600 can be best described as a hard carbon material with abundant, but nearly inaccessible micropores.

The heteroatom content was determined by elemental analysis and is shown in Table 1. With 36 wt% of nitrogen, C-HAT-550 is a nitrogen-rich material rather than a pristine- or classical nitrogen-doped carbon. At higher pyrolysis temperatures the N-content decreased to 6.57 wt% for C-HAT-1000 and 0.41 wt% for C-HAT-1600, that is, typical values for nitrogen-doped carbons. It is already known from previous work that the nitrogen is bound mainly as cyano, pyrazinic, and quaternary nitrogen in C-HAT-550.[25] With increasing carbonization temperature the amount of cyano and pyrazinic groups diminishes and the relative contribution of the quaternary nitrogen is increasing in C-HAT-1000. With an amount of nitrogen as low as 0.41 wt%, C-HAT-1600 can hardly be regarded as nitrogen-doped, as for such low nitrogen contents the impact of adsorbed nitrogen species cannot be ruled out. Chemically it is better described as a rather typical pristine hard carbon with the morphology adapted from the parental material.

Table 1. Pore characteristics of the materials determined from physisorption (Ar at 87 K and CO_2 at 273 K) and elemental composition measured by combustive CHNS analysis.

Sample	$SSA_{BET,Ar}$ [$m^2\ g^{-1}$]	$SSA_{QSDFT,Ar}$ [$m^2\ g^{-1}$]	$V_{CO2(<0.7\ nm)}$ [$cm^3\ g^{-1}$]	*C* [wt%]	*N* [wt%]	*H* [wt%]
C-HAT-550	670	870	0.17	52.35	35.58	1.66
C-HAT-1000	750	770	0.18	89.02	6.57	0.81
C-HAT-1600	20	20	0.13	98.8	0.41	0.15

Powder X-ray diffraction patterns shown in Figure S2, Supporting Information, prove the amorphous structure of C-HAT-550, which shows only a broad reflex at 27°, as it is typical for highly microporous carbon-based materials. In the cases of C-HAT-1000 and C-HAT-1600, a slightly more ordered carbonaceous structure develops with both, the (002) and (100) reflexes being more intense. However, both high-temperature materials still have a diffraction pattern that is characteristic for porous carbon materials. Especially the comparably low 20 $m^2\ g^{-1}$ of SSA detected by Ar physisorption are not at all in line with the shape of XRD pattern of C-HAT-1600. The graphene interlayer distance as estimated from the (002) reflex using Bragg's condition is reduced from 3.8 Å in C-HAT-1000 to 3.7 Å in C-HAT-1600, that is, in both cases well above graphite (3.36 A). The FWHM of the (002) signal slightly decreases at higher synthesis temperatures indicating a slightly improved graphitic-stacking for C-HAT-1600. The two reflexes indicated by asterisks in C-HAT-1600 originate from crystalline SiC contaminations from the high temperature oven.[33] Nonetheless, the small size of the reflexes compared to the carbon signals and the elemental analysis indicate the amount of the impurity to be small.

Raman spectroscopy provides valuable insights into the binding motifs of a carbonaceous material. The Raman spectra of the samples are presented in Figure S3a–d, Supporting Information. Figure S3b–d shows a fit of the region between 900 and 1900 cm^{-1} to a four band model, including the TPA-, D-, A-, and G-bands, following the method of Hu at al.[34,35] With increasing final heat treatment temperature, the TPA- and A- bands decrease in intensity as compared to the D- and G-bands. The former two bands originate from *trans*-polyacetylene bonds and amorphous carbon regions, respectively, while the presence of D- and G-bands indicates a disordered structure dominated by sp^2 carbon. Therefore, it is not surprising to find the D- and G-bands becoming more separated for C-HAT-1000, and to prevail the Raman spectrum of C-HAT-1600 almost entirely.[36,37] Additionally, the presence of the overtones of the D- and G-bands above 2400 cm^{-1} hint at a more ordered structure in the carbon network of C-HAT-1600.[38]

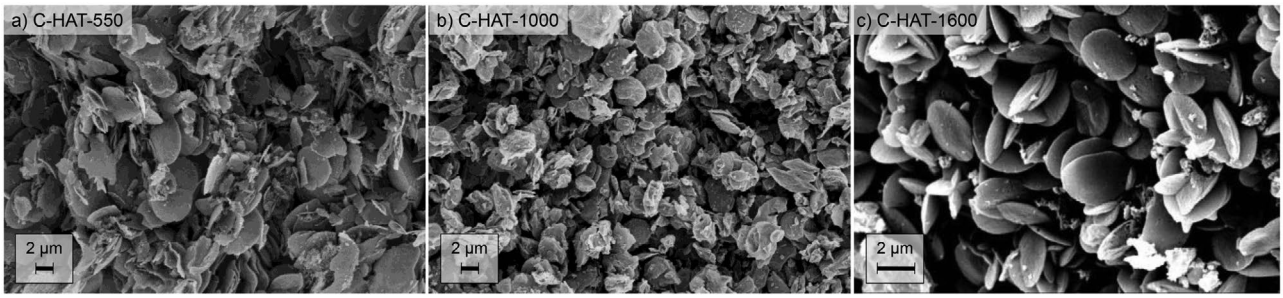

Figure 2. SEM-images of a) C-HAT-550, b) C-HAT-1000, and c) C-HAT-1600.

According to scanning electron microscopy (SEM) images shown in **Figure 2**, the C-HAT keeps their discoid structure throughout all carbonization temperatures. This fact points at a stable, cross-linked network formed during the pyrolysis of the HAT-CN precursor which then undergoes only local structure rearrangements. Further it can be seen that the surface of the C-HAT discs becomes increasingly smooth and the number of fragments decreases for higher pyrolysis temperatures, which is well in line not only with the observed low porosity in C-HAT-1600 determined both by gas sorption. It should be further mentioned that higher conductivity and facilitated electron transport over longer distances is indicated by the higher field emission contrast when doing SEM on C-HAT-1600.

The morphology is kept throughout the carbonization on TEM-scale, as well, as can be seen in the bright-field TEM images in Figure S4, Supporting Information, where all of them show contorted structures on a size scale of a few tens of nanometers.

2.2. Relations between Ar/CO_2 Physisorption and Sodium Storage

In order to get a first impression of the sodium storage characteristics of carbonized HAT-CN materials, charge–discharge curves have been recorded at a current density as low as 18.6 mA g^{-1} in a voltage window between 2.5 and 0 V. Such a low current density enables the study of the charge storage mechanism under equilibrium conditions without running into mass transfer restrictions and other systematic limitations. Typical first and fifth sodiation/desodiation cycles of each studied material are shown in **Figure 3**a, as by the fifth cycle the system is found to be stable and invariant enough to represent the materials' reversible sodiation behavior, the first four cycles are shown in Figure S5, Supporting Information.

All of the materials have in common that the sodiation capacity retention between the first and the first stable cycle is rather low, with retentions between 25% and 34%. This behavior is potentially problematic for the practical application of the material as it would mean a significant loss of electrolyte during the first cycle.

The very high capacity in the first cycle of C-HAT-550 is further noteworthy if viewed outside of the context of subsequent cycles. The first sodiation capacity of C-HAT-550 is almost double that of C-HAT-1000, suggesting a connection between heteroatom content of the materials framework and the first cycle capacity. A significant portion of the current measured during the first cycle is therefore apparently due to SEI-formation including irreversible reactions facilitated by the large nitrogen content of C-HAT-550.

On the other hand, C-HAT-1600 shows an Ar surface area of 20 m^2 g^{-1} but a first sodiation capacity comparable to C-HAT-1000 with an Ar BET-surface area of 750 m^2 g^{-1}. Considering the relatively high CO_2 uptake of both materials it can be concluded that electrolyte molecules and ions are able to enter pores inaccessible to probe gases like Ar and,

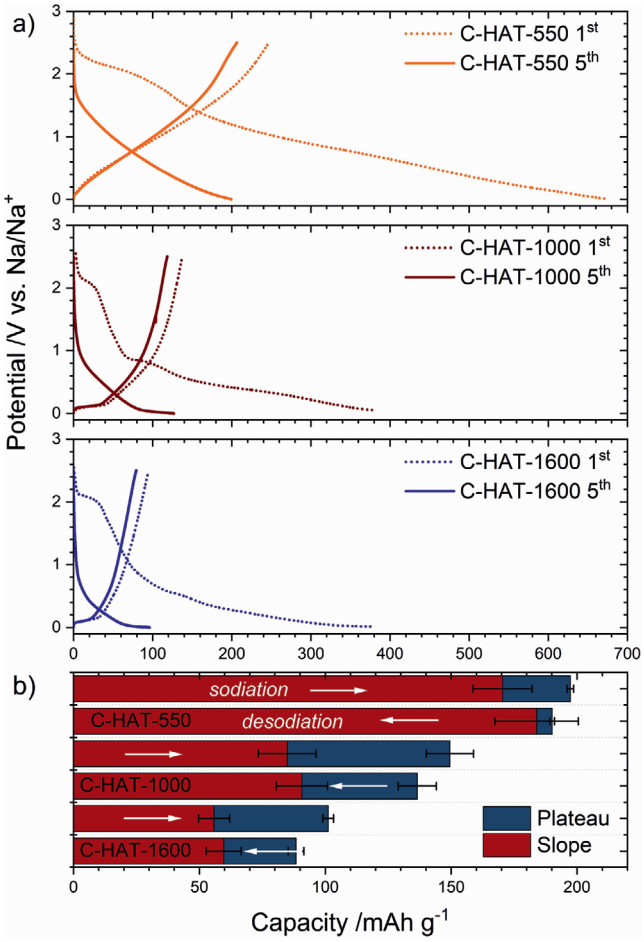

Figure 3. a) Typical first (dotted) and fifth (solid) sodiation/desodiation cycles of C-HAT materials with 0 V as the lower voltage limit at 18.6 mA g^{-1}. b) Mean sodiation and desodiation capacities distinguished into sloping and plateau capacities.

considering the comparable boiling point and molecular dimensions, most likely also N_2 at cryogenic temperatures. Therefore, CO_2 at 273 K is a more suitable probe gas to estimate the "electrochemically active surface area" of such a material during the first cycle. From a physisorption perspective, this is related not only to its slightly smaller kinetic diameter (Ar: 0.34 nm, CO_2: 0.33 nm)[30,39] and higher polarizability, but mainly originates from the higher temperature at which the sorption experiment is conducted. CO_2 has a much higher diffusivity at temperatures as high as 273 K and can reach even the narrowest micropores within a reasonable equilibration time, which is not the case for Ar at 87 K. From a chemical point of view, CO_2 physisorption is suitable to imitate the irreversible processes during SEI formation as CO_2 contains an electrophilic carbon atom and two negatively polarized oxygen atoms comparable in reactivity to the carbonate-based solvent molecules of the electrolyte, which can undergo electron-donor–acceptor interactions with the nitrogen atoms and defect sites of the electrode material. Another important implication arising from the large capacity during the first cycle and the general struggle to relate structural data to electrochemical performance may be that the material obviously undergoes a significant structural change during the first cycle after taking up irreversible capacities of 300 mAh g^{-1} and more: this corresponds to one electrochemical change for 85 mass units. Therefore, the material studied ex situ before the measurement is in fact a different one than the species formed after the first cycle, which is later actually measured as anode material.

Generally, the sodiation curve of hard carbon-like materials is discussed with regard to the sloping and plateau capacities, with different processes taking place at each region. To be able to make this distinction, it is necessary to define "sloping" and "plateau" regions. Following the approach of Xu et al.,[40] a threshold sodiation potential of 0.1 V is defined and all capacity above that value is referred to as sloping and all capacity beneath 0.1 V is referred to as plateau. These values empirically fit the transition from one region to the other very well. While this approach might seem somewhat arbitrary, it is justified by the fact that if the two processes are indeed due to distinct, well defined chemical phenomena, they should take place each at their own defined potential. In the further sections we will discuss why a transition from capacitive to rather faradaic Na storage close to 0.1 V in all hard carbons and hard-carbon like materials is physically reasonable. Last, for the practical use as anode materials, the capacity value below a certain operational voltage is of relevance, as it allows stable battery operation, rendering this approach more application oriented than other methods. Yet, it must be kept in mind that setting a threshold potential carries the possible pitfall of falsely claiming "plateau" capacities for materials with merely a short slope below 0.1 V.

C-HAT-550 shows pure sloping behavior during both, sodiation and desodiation, without a clearly separated voltage plateau. With increasing carbonization temperature the sloping region diminishes from 170 for C-HAT-550 to 85 and 56 mAh g^{-1} for C-HAT-1000 and C-HAT-1600 respectively, and the total sodium storage capacity of the two latter materials decreases. Concomitantly, a plateau begins to emerge for the two latter samples, which is interrupted by the arbitrarily set cut-off voltage of 0 V. This phenomenon is known from the literature[16,41] and can be circumvented by determining the capacity upon which bulk sodium plating occurs (herein called bulk sodium plating capacity), as indicated by a small minimum peak in the charge–discharge curve, and using this capacity as the limit for cycling instead of a voltage limit. This plating capacity value seems to be more suitable for the characterization of an anode material than the capacity at 0 V versus Na/Na^+, because it is a material specific constant and therefore largely independent of error sources like ohmic resistances and other systemic, device-related issues. Indeed, when removing the lower voltage limit and allowing sodiation until bulk metal starts to deposit, C-HAT-550 keeps its exclusively sloping sodiation characteristics, while C-HAT-1000 and C-HAT-1600 continue the sodium uptake at a constant potential until total capacities of 187 and 235 mAh g^{-1} are reached, respectively, as shown in **Figure 4**a. In both materials, sodium storage by intercalation into the expanded graphitic domains as well as possible formation of sodium clusters in the small pores become increasingly dominant.[41,42] This is evident from Figure 4b, where the plateau region contributes 55% (102 mAh g^{-1}) and 76% (179 mAh g^{-1}) to the total capacity.

The change in sodium storage characteristics is clearly due to the structural evolution the material undergoes during heat

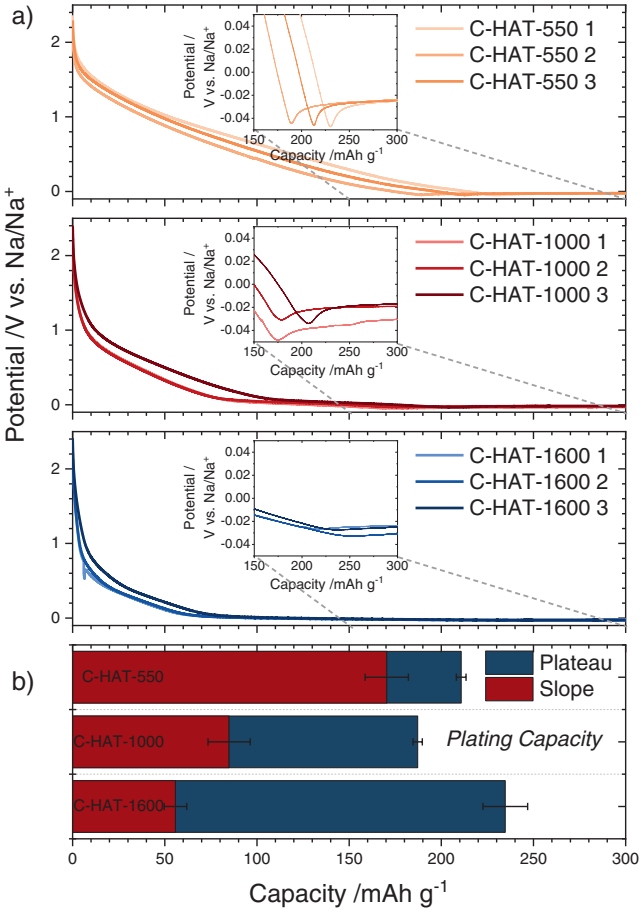

Figure 4. a) Voltage profiles of C-HAT materials during the determination of their bulk sodium plating capacity. b) Bar chart comparing slope and plateau contributions to the plating capacity.

treatment. C-HAT-550 with its high surface area and abundant, narrow micropores can store relatively large amounts of sodium at constantly decreasing potentials with high irreversible capacity. The deposition of sodium does not occur as Na(0) in the materials nanovoids, because sodium is likely to form ionic interactions with the nitrogen-rich, highly polar environment of C-HAT-550. Further, the stabilization of a Na(0) atom requires an appropriate amount of carbon atoms on a preferably defective graphene layer,[43] binding to which the Na(0) atom experiences a similar stabilization energy as the cohesion energy of a sodium crystal or the solvation shell of the surrounding ions.[42] The further growth of such a quasimetallic Na(0) phase however requires an extended, turbostratically disordered and tortuous graphene layer with sufficient lateral dimensions, in order to adsorb to it, forming a 2D layer.

C-HAT-550 is by far a too disordered and defect rich material to provide such an environment. In a binding situation like this, most of the electron density is therefore located in the anode material and sodium in turn is more ionic in nature leading to a charge storage process with rather capacitor-like characteristics, where only a low amount of "stray" Na(0) atoms are present.[44]

At higher synthesis temperatures, nitrogen, in particular pyrazinic and cyano groups, is removed from the material and graphitic domains with enlarged graphene interlayer distances start to form. Notably, the sloping capacity decreases with higher temperature treatment, which can be explained by an ever-lower amount of disordered and polar regions, which tend to adsorb ionic sodium. Instead, sodium can now at slightly lower potentials versus Na/Na^+ adsorb between the formed expanded layers, so that a larger plateau capacity can be observed due to a formed 2D-layer of Na(0). C-HAT-1600 is essentially a hard carbon that inherited the texture and morphology from its starting materials. Its micropores have smaller entrances but are incompletely closed, as indicated by physisorption measurements, where atoms of the size of Ar are locked out at cryogenic temperatures, but smaller and more diffusive species like CO_2 are still able to adsorb. As discussed previously, the still very high first cycle capacity of almost 400 mAh g^{-1} indicates that the electrolyte can reach even those closed pores so that the SEI is also formed there, making it less possible that even those bottleneck-pores to participate in Na(0) storage. Instead, the ever sharper XRD-reflexes indicate a structure of larger turbostratically distorted and bent graphene layers where consequently larger sodium layers can be formed, contributing to the plateau capacity. Where two or more bent graphene layer are found close enough to each other the formed Na(0) layer can, in principle, transform into a cluster like structure—similar to a liquid in a capillary. The potential of these processes is very constant as well as close to the potential, where metallic sodium starts to form, and therefore it hints toward the chemical homogeneity of the formed sodium species.

Another valuable hint at the mechanism of sodium storage is the shape of the peak that precedes the beginning of bulk sodium plating. The signal is considered to represent the crystallization overpotential of sodium crystal nucleation and the height of the peak on the potential-axis is therefore directly related to the crystallization overpotential in the material. The insets in Figure 4a show magnified plots of the potential minimum region in the charge–discharge curve, and the peak height is analyzed in Figure S6 and Table S7, Supporting Information, by subtracting the minimum from the voltage baseline of sodium plating. The peak height significantly decreases from 16.2 mV in C-HAT-550, to 10.1 mV in C-HAT-1000, to finally 1.6 mV in C-HAT-1600. It is thereby evident, that nucleation of sodium is facilitated in materials obtained at higher pyrolysis temperatures, because in such materials a quasimetallic phase is already present at high levels of sodiation and can serve as a nucleus for further growth of extended sodium domains.

As the pores and voids of the C-HAT-materials are never completely closed, the metallic phase can then easily grow out of the pore to form bulk sodium metal. This observation indirectly proves the existence of 2D-Na(0) layers formed in highly sodiated hard carbon anodes.

Cyclic voltammetry measurements can help to clarify the origin of the increased capacity below 0 V. In **Figure 5**, typical CV-cycles of the materials are shown with a lower voltage cutoff of 0 and –0.1 V respectively. Considering first the scan until 0 V, in all three materials a large capacitive contribution is found. The onset of this feature is shifted to lower potentials for materials obtained at higher pyrolysis temperatures and correlates well with the beginning of the sloping regions in the charge–discharge experiments, as it underlines the capacitive nature of the process during the potential slope. Additionally, in C-HAT-1000 and C-HAT-1600 an increasing cathodic current is found at potentials approaching 0 V with its anodic counterpart found at potentials around 0.15 V. When extending the voltage window to –0.1 V, signals proving the presence of two individual processes to appear in both cathodic and anodic scans, labeled with an asterisk and double dagger, respectively. The signal labeled with an asterisk is

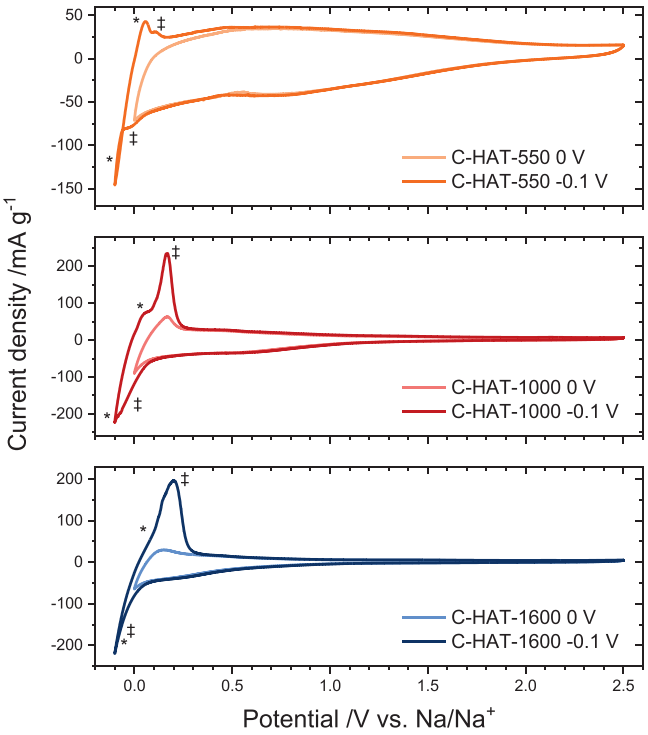

Figure 5. Cyclic voltammetry measurements of C-HAT materials in voltage windows of 0–2.5 V and –0.1–2.5 V at scan rates of 0.1 mV s^{-1}.

most probably due to sodium bulk plating, as it increases steeply and, as it seems, unlimitedly. The signal labeled with a double-dagger however, is due to the same process that forms the plateau region in the charge–discharge curve, namely quasimetallic sodium deposition at graphene layers and in small micropores. The latter seems to appear to a small extent in C-HAT-550, too, as it is evidenced by the presence of a cathodic peak at –0.025 V (double dagger). This was not directly evident from charge–discharge experiments, where no clear plateau could be observed below 0 V. Another remarkable trend observed in the CVs is the gradual coalescence of the plating and micropore deposition peaks with increasing carbonization temperature. While in C-HAT-550 the two signals are clearly distinguishable, they are mere shoulders in the anodic scan of C-HAT-1000 and especially of C-HAT-1600. The fact that the two processes are energetically so close to each other points out that the chemical state of sodium stored in the micropores of hard carbon like materials is very similar to plated sodium metal. It is also possible to comment on the occurrence of sodium intercalation into expanded graphitic regions. As it is known from other alkali ions, intercalation usually takes place a few hundreds of millivolts above the potential of the respective alkali metal.[45] In this work, no significant contribution is found in this voltage range, neither in charge–discharge, nor in CV-experiments. Contrary, the capacity contribution above 0 V is reducing with an expansion of the graphene interlayer distance and the main capacity is found around or lower than 0 V, which indicates against sodium intercalation as the source of the plateau.

To prove the reversibility and applicability of the capacity limitation method, all three materials were cycled to 90% of their respective bulk sodiation capacity for five cycles, after being initially cycled to a voltage limit of 0.002 V and the corresponding results are presented in **Figure 6**. The bulk sodiation capacity was previously determined as the arithmetic mean of three separate measurements of the minimum of the crystallization overpotential peak, like discussed in Figure 4. Reversible behavior in the sodiation/desodiation curves were measured for all of the materials, however, a significant increase in sodium storage capacity is only measured in materials with a considerable plateau capacity below 0 V, when this approach is used. For C-HAT-550, which starts to plate bulk metal sodium almost immediately after reaching 0 V, some capacity remains unutilized, because in this material 90% of the bulk plating capacity is reached above a potential of 0 V.

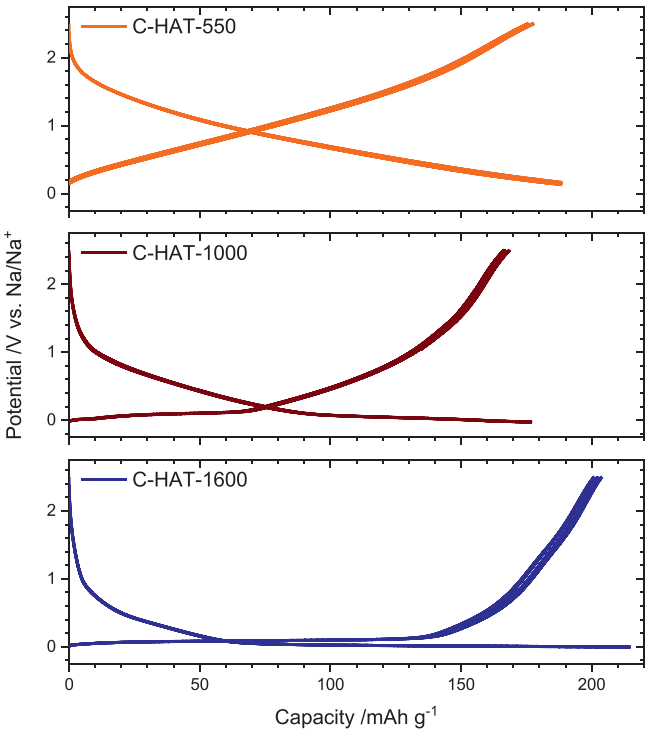

Figure 6. Voltage profiles of C-HAT materials cycled with 18.6 mA g^{-1} until 90% of their respective bulk sodium plating capacity. A reversible behavior is observed over five subsequent cycles.

From these measurements, it is evident, that C-HAT-1600 is the most suitable SIB-anode material among the three samples. It shows not only the highest capacity, but most importantly, most of the capacity is available at a low and constant voltage, which is beneficial for the application as an anode material. A profound knowledge about the origin of this high plateau capacity is needed to allow for future targeted enhancement of carbon-based materials for sodium ion batteries. Therefore, C-HAT-1600 will be investigated in more detail in the next chapter.

2.3. C-HAT-1600 as a Promising SIB Anode Material

The potential application of C-HAT-1600 with its 235 mAh g^{-1} of capacity and a particularly low potential plateau capacity of 179 mAh g^{-1} as an SIB anode material was further evaluated. To do so, its performance at higher currents as well as its long-term cyclability was assessed using the capacity-limited approach. As the bulk sodium plating capacity is dependent on the current applied, it has to be determined for each current value separately. Currents of 18.6, 74.4, and 186 mA g^{-1}, corresponding to C/20, C/5, and C/2 of a Li-graphite anode were chosen and the results of the plating capacity determination are shown in **Figure 7**a,b. When the current density is increased from C/20 to C/5 only a small decrease in capacity of about 35 mAh g^{-1} can be observed. At a current density of C/2 however, the capacity drops to ≈100 mAh g^{-1}. Generally, the plateau capacity is less pronounced at higher current densities.

With the bulk sodiation capacities known, the material was cycled to 95% of the determined value. The results are presented in Figure 7c,d and suggest that the cell can be cycled even at higher current densities with a sufficiently high coulombic efficiency and most importantly without the risk of plating bulk sodium. The results of the long term cycling at C/2 support this observation, here C-HAT-1600 shows a coulombic efficiency significantly greater than 99%, especially once the cell is cycled in. Overall, even though C-HAT-1600 is not a record-breaking SIB anode material it demonstrates the viability and operational safety of the capacity limitation approach.

3. Conclusion

The sodium storage mechanism in hard carbon like materials has been studied on materials derived from the organic,

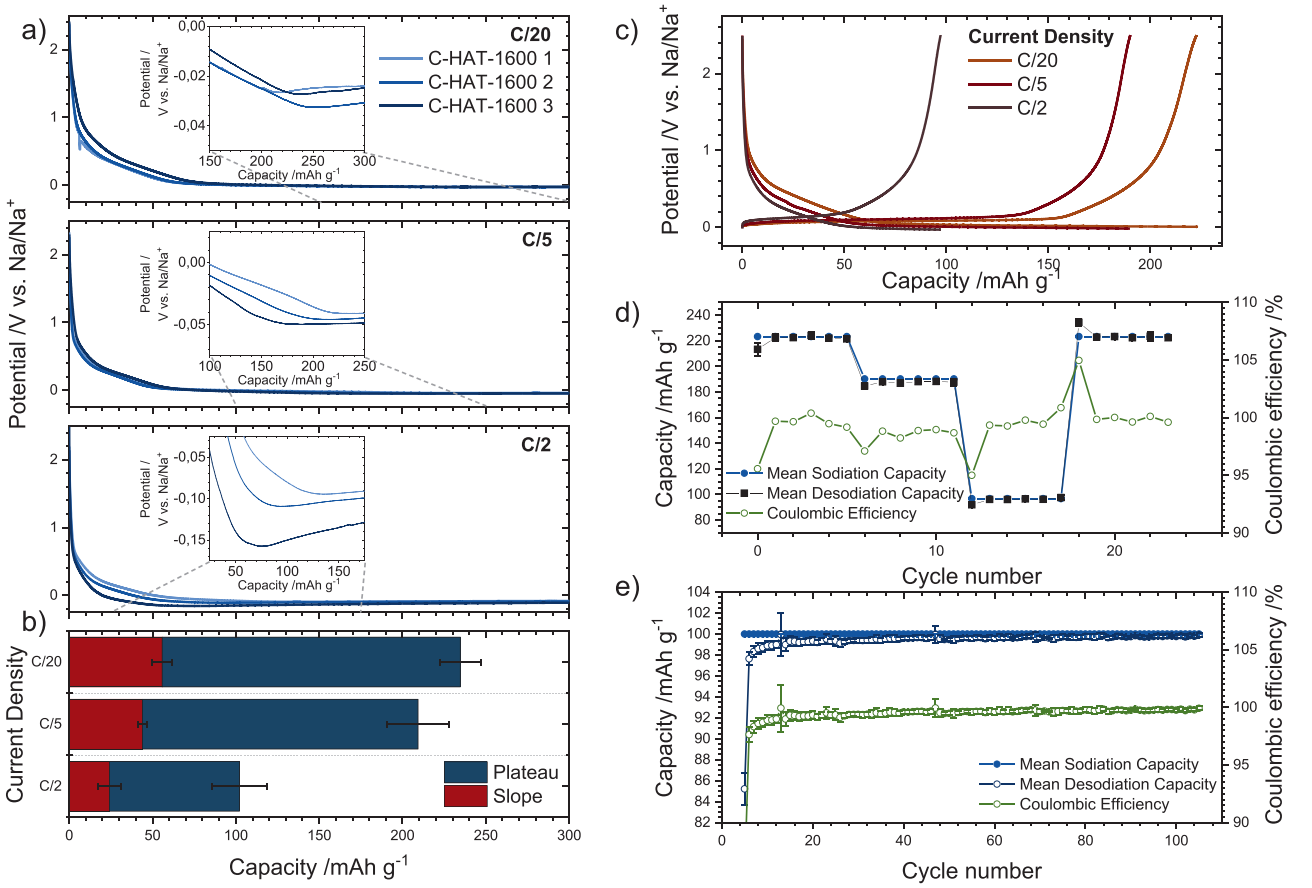

Figure 7. Characterization of C-HAT-1600 as an SIB-anode material. a) Determination of the bulk sodium plating capacity at C/20, C/5, and C/2. b) Bar chart comparing slope and plateau contributions to the plating capacity at C/20, C/5, and C/2. c) Charge–discharge profiles at different current densities with capacity limitation. d) Capacity and coulombic efficiency of C-HAT-1600 at different current densities. e) Cycling at C/2 over 100 cycles.

self-templating hard carbon precursor HAT-CN as a function of their pore structure and chemical composition. As a significant part the materials capacity can be only utilized at potentials lower than 0 V versus Na/Na^+, the conventional charge–discharge protocol with constant current applied in a voltage range between 2.5 and 0.002 V was modified to a capacity limited approach. In this method, the sodiation capacity is viewed as a material specific amount of sodium that can be taken up, before bulk sodium begins to crystallize. This approach can in principle be applied not only to carbons, but to any material stable in the respective voltage range and reflects the storage capabilities in a physically more meaningful way than the established voltage limited experiment. Though, the experimental effort is significantly higher, as several cells must be sacrificed in order to determine the bulk sodiation capacity prior to cycling. It was found that the sloping capacity region diminishes in materials synthesized at high temperatures, where the heteroatom content decreases and the degree of order increases. Contrary, the capacity plateau emerging due to the insertion of sodium into expanded graphite domains and particularly the formation of 2D-sodium layers in high temperature-derived materials where sodium is bound in zero-charge form with metallic-bonded Na(0) neighbors stabilized by graphene layers at a constant potential. Based on our results, we propose such sodium layers to be the first stage of the deposition of Na(0) in hard carbon anodes. In regions of the carbon, where the graphene layers form small, internal, pore-like structures, the deposited layer can coalesce and form a cluster, so our understanding is in line previous models of pore filling during the plateau region. At the same time the overpotential required to nucleate bulk sodium is decreasing with increasing carbonization temperatures, indicating that sodium layers formed at high degrees of sodiation can serve as nuclei for the growth of expanded domains, once the materials sodiation capacity is exhausted. The results are further confirmed by cyclic voltammetry measurements, which have proven as a very useful technique for the characterization of such phenomena. From a comparison of electrochemical and physisorption data it was found that sodium ions as well as molecules constituting the SEI can still access pores that Ar atoms cannot enter and even data from CO_2 sorption at 273 K can serve only as an indication for the extent of SEI formation in the first cycle. Na(0) storage beyond the deposition in layers at graphene domains however can only be accomplished by truly closed pores, accessible only to sodium and only via solid state diffusion through the carbon material. It follows that it might be meaningful to regard those pores not as pores in the classical physisorption sense, but more as hard carbon-specific defects, understanding the nature of which would enable

safe and efficient sodium storage in SIB anodes. Further work might include advanced scattering techniques, combined with tailored in-depth analysis methods, as to our view these are best suitable to study the dynamic and highly sensitive alkali-ion/hard carbon system. Electron microscopic imaging, as well as magnetic resonance techniques could serve well in the understanding of ion storage in hard carbons.

4. Experimental Section

Synthesis of Carbon Materials: Hexaazatriphenylenehexacarbonitrile (HAT-CN) was synthesized following the procedure of Rademacher et al.[46] HAT-CN was heated in a horizontal tube furnace under Ar atmosphere according to the method of Walczak et al.[25] to obtain carbon materials with different porosities and heteroatom contents. In particular, HAT-CN was first heated to 60 °C at a heating rate of 4 °C min^{-1} and held for 30 min. In the second heating step, the material was heated to the target temperature of 550 or 1000 °C with 4 °C min^{-1} and held for 60 min. The materials were denoted as C-HAT-550 and C-HAT-1000. C-HAT-1600 was obtained by transferring C-HAT-1000 into a high-temperature horizontal tube furnace and subjecting it to a further heat-treatment in Ar-atmosphere at 1600 °C for 60 min with a ramp of 3 °C min^{-1}.

Structural Characterization: Gas physisorption measurements were conducted on a Vapor200C gas sorption analyzer by 3P Instruments. Ar at −186 °C, and CO_2 at 0 °C were used as probe gases. The samples were degassed under vacuum at 150 °C for at least 20 h before each measurement. Specific surface areas were calculated from the adsorption branch by the multipoint BET-method as well as by quenched solid density functional theory (QSDFT) from the adsorption branch of the Ar isotherm for slit/cylindrical shaped carbon pores. The same QSDFT kernel was used to calculate the pore size distributions.[30,47]

The nitrogen, carbon, and hydrogen content were determined from combustive elemental analysis (EA) on a vario MICRO elemental analyzer by Elementar.

X-ray diffraction patterns were recorded on a Bruker D8 in Bragg-Brentano geometry in a 2Θ range of 10°–70° with a resolution of 0.03° with $Cu_{K\alpha}$ radiation ($\lambda = 0.154$ nm) and a NaI scintillation detector. The samples were placed on a horizontal silicon single crystal holder.

SEM Images were recorded on a LEO 1550-Gemini microscope at 3 kV acceleration voltage and on a JEOL JSM-6510 with an acceleration voltage of 8 kV. Samples were sputtered with platinum or a gold/palladium alloy before each measurement.

HRTEM images were measured on a JEOL ARM 200F microscope operating at 80 or 200 kV of acceleration voltage, respectively. The samples were prepared by dispersing the powder in ethanol and casting several droplets of the dispersion onto copper TEM grids with holey carbon films, before drying them at room temperature.

Raman spectra were measured on a Witec Raman Microscope with an excitation wavelength of 532 nm at an intensity of 3.5 mW and a Nikon objective (10×/0.25, ∞/−WD 6.1).

Electrochemical Characterization: The carbon materials were fabricated into inks by grinding them together with carbon black (SuperP, Alfa Aesar) as the conductive additive and adding an aqueous solution of carboxymethylcellulose as the binder in the mass ratio of 8:1:1. The ink was sonicated for 1 h and stirred overnight, before it was coated on copper foils (Alfa Aesar, 99.8%, 0.025 mm thickness) of 10 mm in diameter to achieve an area loading of ≈1 mg cm^{-1}.The electrodes were dried under vacuum at 60 °C prior to usage in sodium-ion half-cells. The electrochemical measurements were performed in 2-electrode Swagelok-type cells on a Biologic MPG-2 potentiostat. 300 µL of a 1 M solution of $NaPF_6$ in a 6:4 v/v mixture of ethylene carbonate and diethyl carbonate were used as the electrolyte in each cell. Whatman GF/C glassfiber filters served as the separators and a thin piece of sodium metal acted as both, the counter and reference electrode. Potentials were always referred to as against Na/Na^+, unless otherwise stated.

For the sake of comparability, the current density was set with respect to of a Li-graphite anode, where 1 C corresponds to 372 mA g^{-1}. Charge–discharge curves were recorded in two different modes using: i) voltage limitation between 2.5 and 0.002 V; and b) a lower capacity limit of 90% of the previously determined bulk sodium plating capacity at C/20. The plating capacity was measured three times at C/20 for each material and an arithmetic mean value was calculated.

For C-HAT-1600, plating capacities were additionally determined at C/5 and C/2 in order to test its rate capability. Then, the material was cycled in for 5 cycles between 2.5 and 0.002 V and then current densities of C/20, C/5, and C/2 were applied for 5 cycles each to a lower capacity limit of 90% of the respective sodium plating capacity. Long term cycling was performed for C-HAT-1600 in capacity-limited mode as well at C/2 for 100 cycles.

Cyclic voltammetry (CV) was measured in a voltage range of 0.0–2.5 V and −0.1–2.5 V at a scan rate of 0.1 mV s^{-1}.

Supporting Information

Supporting Information is available from the Wiley Online Library or from the author.

Acknowledgements

Financial support within the Max Planck-Fraunhofer Cooperation programme (CLUSTERBATT) is gratefully acknowledged. The authors thank Antje Völkel and Heike Runge for the careful conduction of elemental analyses and scanning electron microscopy, respectively. The authors further thank Dr. Nadja Tarakina and Bolortuya Badamdorj for measurement of TEM images. Experimental assistance by Marcus Pieper and Cevin Braksch is gratefully acknowledged.

Open access funding enabled and organized by Projekt DEAL.

Conflict of Interest

The authors declare no conflict of interest.

Data Availability Statement

The data that support the findings of this study are available from the corresponding author upon reasonable request.

Keywords

energy storage, hard carbons, Na-ion batteries, pore structures, anodes

Received: October 29, 2020
Revised: January 21, 2021
Published online: February 22, 2021

[1] A. Manthiram, *ACS Cent. Sci.* **2017**, *3*, 1063.
[2] Y. You, A. Manthiram, *Adv. Energy Mater.* **2018**, *8*, 1701785.
[3] X. Xiang, K. Zhang, J. Chen, *Adv. Mater.* **2015**, *27*, 5343.
[4] X. Dou, I. Hasa, D. Saurel, C. Vaalma, L. Wu, D. Buchholz, D. Bresser, S. Komaba, S. Passerini, *Mater. Today* **2019**, *23*, 87.
[5] R. J. Clément, P. G. Bruce, C. P. Grey, *J. Electrochem. Soc.* **2015**, *162*, A2589.
[6] C. Delmas, J.-J. Braconnier, C. Fouassier, P. Hagenmuller, *Solid State Ionics* **1981**, *3–4*, 165.

[7] M. Chen, Q. Liu, Z. Hu, Y. Zhang, G. Xing, Y. Tang, S. L. Chou, *Adv. Energy Mater.* **2020**, *10*, 2002244.
[8] M. Chen, J. Xiao, W. Hua, Z. Hu, W. Wang, Q. Gu, Y. Tang, S. L. Chou, H. K. Liu, S. X. Dou, *Angew. Chem., Int. Ed.* **2020**, *59*, 12076.
[9] B. Jache, P. Adelhelm, *Angew. Chem., Int. Ed.* **2014**, *53*, 10169.
[10] Y. Wen, K. He, Y. Zhu, F. Han, Y. Xu, I. Matsuda, Y. Ishii, J. Cumings, C. Wang, *Nat. Commun.* **2014**, *5*, 4033.
[11] M. Hu, H. Zhou, X. Gan, L. Yang, Z. H. Huang, D. W. Wang, F. Kang, R. Lv, *J. Mater. Chem. A* **2018**, *6*, 1582.
[12] Y. J. Kang, S. C. Jung, J. W. Choi, Y. K. Han, *Chem. Mater.* **2015**, *27*, 5402.
[13] B. E. Conway, *Electrochemical Supercapacitors: Scientific Fundamentals and Technological Applications*, Springer Science+Business Media, New York, NY, **1999**.
[14] C. Costentin, J. M. Savéant, *Chem. Sci.* **2019**, *10*, 5656.
[15] M. B. Armand, in *Materials for Advanced Batteries* (Eds: D.W. Murphy, J. Broadhead, B.C.H. Steele), Plenum Press, New York, NY, **1980**, pp. 145–162.
[16] Y. Zheng, Y. Lu, X. Qi, Y. Wang, L. Mu, Y. Li, Q. Ma, J. Li, Y. S. Hu, *Energy Storage Mater.* **2019**, *18*, 269.
[17] Y. Matsukawa, F. Linsenmann, M. A. Plass, G. Hasegawa, K. Hayashi, T.-P. Fellinger, *Beilstein J. Nanotechnol.* **2020**, *2020*, 1217.
[18] M. Sevilla, A. B. Fuertes, *Carbon* **2009**, *47*, 2281.
[19] M. M. Titirici, A. Thomas, S. H. Yu, J. O. Müller, M. Antonietti, *Chem. Mater.* **2007**, *19*, 4205.
[20] A. C. S. Jensen, E. Olsson, H. Au, H. Alptekin, Z. Yang, S. Cottrell, K. Yokoyama, Q. Cai, M. M. Titirici, A. J. Drew, *J. Mater. Chem. A* **2020**, *8*, 743.
[21] S. Wenzel, T. Hara, J. Janek, P. Adelhelm, *Energy Environ. Sci.* **2011**, *4*, 3342.
[22] D. Li, H. Chen, G. Liu, M. Wei, L. X. Ding, S. Wang, H. Wang, *Carbon* **2015**, *94*, 888.
[23] X. Zhou, X. Zhu, X. Liu, Y. Xu, Y. Liu, Z. Dai, J. Bao, *J. Phys. Chem. C* **2014**, *118*, 22426.
[24] M. S. Balogun, Y. Luo, W. Qiu, P. Liu, Y. Tong, *Carbon* **2016**, *98*, 162.
[25] R. Walczak, B. Kurpil, A. Savateev, T. Heil, J. Schmidt, Q. Qin, M. Antonietti, M. Oschatz, *Angew. Chem., Int. Ed.* **2018**, *57*, 10765.
[26] J. L. Segura, R. Juárez, M. Ramos, C. Seoane, *Chem. Soc. Rev.* **2015**, *44*, 6850.
[27] X. Y. Yan, M. Di Lin, S. T. Zheng, T. G. Zhan, X. Zhang, K. D.a Zhang, X. Zhao, *Tetrahedron Lett.* **2018**, *59*, 592.
[28] R. Yan, E. Josef, H. Huang, K. Leus, M. Niederberger, J. P. Hofmann, R. Walczak, M. Antonietti, M. Oschatz, *Adv. Funct. Mater.* **2019**, *29*, 1902858.
[29] R. Yan, K. Leus, J. P. Hofmann, M. Antonietti, M. Oschatz, *Nano Energy* **2020**, *67*, 104240.
[30] J. Silvestre-Albero, A. Silvestre-Albero, F. Rodríguez-Reinoso, M. Thommes, *Carbon* **2012**, *50*, 3128.
[31] M. Thommes, K. Kaneko, A. V. Neimark, J. P. Olivier, F. Rodriguez-Reinoso, J. Rouquerol, K. S. W. Sing, *Pure Appl. Chem.* **2015**, *87*, 1051.
[32] C. Matei Ghimbeu, J. Górka, V. Simone, L. Simonin, S. Martinet, C. Vix-Guterl, *Nano Energy* **2018**, *44*, 327.
[33] J.-M. Nhut, L. Pesant, N. Keller, C. Pham-Huu, M. J. Ledoux, *Top. Catal.* **2004**, *30/31*, 353.
[34] C. Hu, S. Sedghi, A. Silvestre-Albero, G. G. Andersson, A. Sharma, P. Pendleton, F. Rodríguez-Reinoso, K. Kaneko, M. J. Biggs, *Carbon* **2015**, *85*, 147.
[35] M. W. Smith, I. Dallmeyer, T. J. Johnson, C. S. Brauer, J. S. McEwen, J. F. Espinal, M. Garcia-Perez, *Carbon* **2016**, *100*, 678.
[36] A. C. Ferrari, J. Robertson, *Phys. Rev. B: Condens. Matter Mater. Phys.* **2001**, *64*, 075414.
[37] A. C. Ferrari, J. Robertson, *Phys. Rev. B* **2000**, *61*, 14095.
[38] A. C. Forse, C. Merlet, P. K. Allan, E. K. Humphreys, J. M. Griffin, M. Aslan, M. Zeiger, V. Presser, Y. Gogotsi, C. P. Grey, *Chem. Mater.* **2015**, *27*, 6848.
[39] N. Mehio, S. Dai, D. Jiang, *J. Phys. Chem. A* **2014**, *118*, 1150.
[40] F. Xu, Y. Qiu, H. Han, G. Jiang, R. Zhao, E. Zhang, H. Li, H. Wang, S. Kaskel, *Carbon* **2020**, *159*, 140.
[41] Y. Morikawa, S. Ichi Nishimura, R. Ichi Hashimoto, M. Ohnuma, A. Yamada, *Adv. Energy Mater.* **2020**, *10*, 1903176.
[42] C. Bommier, T. W. Surta, M. Dolgos, X. Ji, *Nano Lett.* **2015**, *15*, 5888.
[43] P. C. Tsai, S. C. Chung, S. K. Lin, A. Yamada, *J. Mater. Chem. A* **2015**, *3*, 9763.
[44] J. M. Stratford, P. K. Allan, O. Pecher, P. A. Chater, C. P. Grey, *Chem. Commun.* **2016**, *52*, 12430.
[45] Y. Li, Y. Lu, P. Adelhelm, M. M. Titirici, Y. S. Hu, *Chem. Soc. Rev.* **2019**, *48*, 4655.
[46] J. T. Rademacher, K. Kanakarajan, A. W. Czarnik, *Synthesis* **1994**, *1994*, 378.
[47] G. Y. Gor, M. Thommes, K. A. Cychosz, A. V. Neimark, *Carbon* **2012**, *50*, 1583.